Draft manuscript for International Journal of Plasticity

Mechanism-based modeling of thermal and irradiation creep behavior: an application to Ferritic/Martensitic HT9 steel

W. Wen[1], A. Kohnert[2], M. Arul Kumar[2*], L. Capolungo[2], C.N. Tomé[2]

[1]Department of Engineering, Lancaster University, Lancaster, LA1 4YR, UK

[2]Materials Science and Technology Division, Los Alamos National Laboratory
Los Alamos, NM 87544, USA

Abstract

In this work, the creep behavior of HT9 steel in both thermal and irradiation environments is predicted using an integrated modeling framework. Multiple physical mechanisms such as diffusional creep and dislocation climb are incorporated into crystal plasticity calculations using the Visco-Plastic Self-Consistent (VPSC) approach. Climb velocities are informed by mean field rate theory laws in place of empirical power law formulations. More interestingly, the climb velocities explicitly consider the contribution of irradiation-induced point defects, i.e., stress induced preferential absorption (SIPA) effect. The developed expressions are shown to apply under conventional thermal creep and to the more complex irradiation conditions as well. This physically-informed, mechanism-based model is used to simulate the creep strain evolution of HT9 pressurized tubes under various loading conditions. It is demonstrated that the experimental behavior of this material reported in the literature is well described by this theoretical framework. The role of each relevant mechanism is discussed.

Keywords: thermal creep, irradiation creep, HT9 steel, crystal plasticity

1 Introduction

High Cr steels are being considered as candidates for the next generation cladding material in nuclear reactors. This material shows low swelling rates under neutron

irradiation and high-temperature creep strength, which effectively enhances the accident tolerance and reliability of the reactors. The irradiation creep behavior and microstructure evolution in Fe-Cr alloys have been investigated experimentally (Anderoglu et al., 2012; Chen et al., 2015; Garner, 1994; Maloy et al., 2016; Rogozhkin et al., 2016; Sencer et al., 2009; Zheng et al., 2017). Meanwhile, modeling work has received disproportionally less attention, and most models proposed thus far are semi-empirical, i.e. heavily relying on the fitting of macroscopic experimental data at a given temperature, radiation dose and stress (Pastore et al., 2015; Uehira et al., 2000). Overall material relaxation (e.g. creep) depends on stress, temperature and irradiation flux and dose, and constitutive laws with better predictive capability are essential for two reasons. First, creep and swelling rates show strong sensitivities to the material service history (thermomechanical process and irradiation exposure) (Garner, 1994; Sencer et al., 2009). Thus, it is important for models to track microstructure evolution during in-service operation and to describe precisely its effect on the material properties. Second, under abnormal operation or accident situations, the material experiences conditions that deviate substantially from the steady state ones used to fit empirical models. The rate controlling processes will evolve as a function of environments, and such evolution cannot be captured using macroscopic empirical laws. Therefore, using empirical material behavior models in technologic applications requires one to increase the safety factors being used, and constrains the application to operational conditions that have been previously tested experimentally. As such, it is desirable to be able to extrapolate beyond the test conditions used when the materials are expected to serve under complex and sometimes uncertain environments.

Mechanism-based models that focus on the deformation mechanisms at the grain scale level are key to reaching predictive capabilities that can address general loading histories and evolving conditions. The development of such models requires a deeper understanding of the relevant plastic deformation mechanisms and their associated effects on microstructure evolution for the material in question. In particular, irradiation-induced precipitation has been intensively studied as it is strongly related to the degradation of materials performance and premature failure in cladding materials (irradiation embrittlement). Cr-rich α' precipitates are commonly observed in irradiated Fe-Cr alloys,

although their formation is prevented at temperatures higher ~460$_0$C (Anderoglu et al., 2012; Kai and Klueh, 1996). The presence of Al as an alloying element may also destabilize the boundaries of the α' phase and decelerate precipitation (Briggs et al., 2017; Edmondson et al., 2016; Field et al., 2016; Field et al., 2015). G-phase particles ($M_6Mn_{16}Si_7$) are also an important hardening source under irradiation temperatures in the 400°C to 500°C range (Anderoglu et al., 2012; Sencer et al., 2009; Zheng et al., 2017). Other precipitates, such as M_2X, η (M_6X) and χ (intermetallic phase), are also detected (Dubuisson et al., 1993; Getto et al., 2017; Kai and Klueh, 1996). The MX carbo-nitride and $M_{23}C_6$ carbide are reported in several studies (Kai and Klueh, 1996; Sencer et al., 2009; Zheng et al., 2017). However, they are likely to be generated during heat-treatment and thermo-mechanically processing and their size and number densities do not change significantly under irradiation. Moreover, the irradiation-induced formation of voids and loops (<111> type predominate) have also been quantified in experimental studies (Briggs et al., 2017; Field et al., 2016; Field et al., 2015; Getto et al., 2017). All of these features contribute to hardening and creep resistance by acting as obstacles to dislocation slip.

Below the yield point, plastic deformation occurs by processes mediated by point defect transport. Of these, a crucial mechanism is climb, whereby dislocations absorb or emit point defects resulting in non-conservative motion. Climb contributes directly to plastic deformation but also allows obstacle bypass resulting in incremental slip below the yield point. Irradiation creates a super-saturation of vacancies and self-interstitials, which can modify the kinetics of dislocation climb relative to a thermal environment where only the equilibrium vacancy population is available. Interactions between the internal stresses produced by dislocations and externally applied loads modify the absorption kinetics of point defects on different slip systems, a mechanism for creep known as stress induced preferential absorption (SIPA). The origins of this effect are ambiguous, and may stem from a second order strain dependence in defect formation energy (diaelastic polarizability) or from coupling to defect elasto-diffusion (Bullough and Willis, 1975; Woo, 1984). The creep behavior of irradiated metals takes contributions from both the SIPA effect as well as the typical behaviors activated during thermal creep, with magnitudes that depend on microstructure, exposure conditions, and temperature. Interestingly though, climb

processes originating from thermal and irradiation contributions can be quantified together using the mean field rate theory approach (Matthews and Finnis, 1988). Doing so self-consistently captures the effect of both the mechanical (Peach-Koehler) and chemical (Bardeen-Herring) forces, producing a physically based law for climb based plasticity accounting for stress, temperature and irradiation effects. Such law can be applied in place of empirically calibrated power-law formulations for climb (Lebensohn et al., 2010) and also avoid the use of phenomenological irradiation creep model (Ehrlich, 1981; Foster et al., 1972).

The purpose of this work is to develop a mechanism-based model to capture the thermal and irradiation creep behavior of Fe-Cr alloys. Specifically, HT-9 (Fe-12Cr-1Mo) steel is chosen as the model material. This model adheres to a harmonic transition state theory based framework originally proposed by Wang et al. (Wang et al., 2017; Wang et al., 2016) to describe the heterogeneous distribution of internal stresses in each grain. The local strain-stress response includes a hardening law (Soare and Curtin, 2008a, b; Wen et al., 2018) to describe the dislocation mobility with the presence of solute atoms, accounting for the effects of the solute diffusion around the dislocation core. This core-diffusion law shows promising results in the prediction of the thermal creep behavior and anomalous strain rate sensitivity in Zr alloy (Wen et al., 2018). Besides the core-diffusion, the proposed model also incorporates a novel rate theory-based law for dislocation climb considering the contribution of irradiation-induced point defects. This model, which is embedded in the crystallographic visco-plastic self-consistent (VPSC) framework (Lebensohn et al., 2007; Lebensohn and Tome, 1993), will be introduced in section 2. The simulation results for thermal and irradiation creep of HT-9 are analyzed and compared to the data of Toloczko et al. (Toloczko et al., 2001) in section 3, followed by the conclusion in section 4.

2 Crystal plasticity-based creep model

The proposed physics-based model developed aims to capture the thermal and irradiation creep behaviors of HT-9. This work is based on the constitutive model proposed in previous studies considering Coble creep and solute strengthening related mechanisms

(Wen et al., 2018). A new law describing dislocation climb effects is proposed. The total creep rate can be expressed as:

$$\dot{\varepsilon}^p = \dot{\varepsilon}^d + \dot{\varepsilon}^c + \dot{\varepsilon}^{coble} \quad (1)$$

$\dot{\varepsilon}^d$, $\dot{\varepsilon}^c$ and $\dot{\varepsilon}^{coble}$ refer to the plastic deformation accumulated through dislocation glide, climb and Coble creep, respectively. The strain rates due to dislocation motion can be written as the sum of the mean shear/climb rates over all active systems in the grain:

$$\dot{\varepsilon}^d = \sum_s m_{ij}^s \bar{\dot{\gamma}}^s \quad \text{and} \quad \dot{\varepsilon}^c = \sum_s c_{ij}^s \bar{\dot{\beta}}^s \quad (2)$$

Here $\bar{\dot{\gamma}}$ and $\bar{\dot{\beta}}$ denote the mean shear and climb rates, respectively. $\boldsymbol{m}^s$is the symmetric part of the Schmid tensor. $\boldsymbol{c} = (\boldsymbol{b}^s \otimes \boldsymbol{b}^s)$ is the climb tensor for edge dislocations (Lebensohn et al., 2010).

This model relies on the original work of Wang et al. (Wang et al., 2017; Wang et al., 2016) in which the response of each material point (grain) is described in a statistical fashion (i.e. via the internal stress distribution) to allow the quantification of type III stresses associated with dislocations. With this approach, one must calculate the average strain rate in one grain accounting for the mechanical response in all sub-material points. This treatment provides a connection between the localized stress distribution within sub-material point and the average response of the material point.

It is also required by the effective medium models, such as the VPSC framework, that assume the strain rate and stress within each grain are homogenous. As per Wang et al. (Wang et al., 2017; Wang et al., 2016), the mean shear rate of the slip system s in the grain domain is expressed as:

$$\bar{\dot{\gamma}}^s = \int_{-\infty}^{\infty} \dot{\gamma}^s(\tau^s)\ P(\tau^s - \bar{\tau}^s) d\tau^s \quad (3)$$

Where $\dot{\gamma}^s$ is the shear rate of one sub-material point. τ^s is the local resolved shear stress. $\bar{\tau}^s = \boldsymbol{\sigma} : \boldsymbol{m}^s$ denotes the mean resolved shear stress in one grain, where $\boldsymbol{\sigma}$ is the deviatoric stress tensor. Notice that this law applies to the climb rate as well:

$$\bar{\dot{\beta}}^s = \int_{-\infty}^{\infty} \dot{\beta}^s(\tau^s_{climb})\ P(\tau^s_{climb} - \bar{\tau}^s_{climb}) d\tau^s_{climb} \tag{4}$$

with τ^s_{climb} and $\bar{\tau}^s_{climb} = \boldsymbol{\sigma} : \boldsymbol{c}^s$, being the local and global resolved climb stress, respectively.

Historically, internal stress distributions and their relationships with dislocation content have been investigated through line profile analysis (Groma and Bakó, 1998; Groma and Székely, 2000; Wilkens, 1970). As a first approximation, each component of the stress field can be described by a Gaussian function. Therefore, the probability distribution function $P(\tau^s - \bar{\tau}^s)$, representing the volume fraction of sub-material points with τ^s, can be written as:

$$P(\tau^s - \bar{\tau}^s) = \frac{1}{\sqrt{2\pi V}} \exp\left(-\frac{(\tau^s - \bar{\tau}^s)^2}{2V^2}\right) \tag{5}$$

here V is the distribution variance. Wang et al. (Wang et al., 2016) suggest that the dispersion of intragranular stress depends on the total dislocation density, and express V as:

$$V = \eta\sqrt{\rho_{cell} + \rho_{cw}} \tag{6}$$

Where $\eta \sim 10^7$ MPa/m is an effective scaling coefficient, introduced here for the sake of simplicity. In practice, though, η is expected to be a function depending on the 'Contrast factor' for each dislocation population and on dislocation arrangements. As such, Eq. (6) should be considered a coarse estimate of the connection between dislocation content and variance in the stress distributions (Wang et al., 2017; Wang et al., 2016). ρ_{cell} and ρ_{cw} are the total dislocation densities in the cell (subgrain) interior and in the cell walls (subgrain boundaries), respectively. The dislocation density evolution laws will be introduced below. Notice that the subgrain size effect is accounted for implicitly in the internal stress distribution given by Eq. (6), as the subgrain size (λ_{sg}) can be related to ρ_{cw} as we discuss in Sec. 2.3.

2.1 Dislocation glide

In this model, the local shear rate on system s can be expressed using the Orowan's equation:

$$\dot{\gamma}^s = \rho_{cell}^s b^s v^s \operatorname{sign}(\tau^s) \tag{7}$$

here $\operatorname{sign}(\tau^s)$ enforces the direction of the shear rate to be the same as the direction of glide. b^s is the magnitude of the Burgers vector. v^s is the mean dislocation velocity, which can be determined from the mean spacing between obstacles (dislocation mean free path, λ^s) and the time a dislocation spends traveling between obstacles, given by the sum of the waiting time at obstacles (t_w^s) and the travel time within the interspacing (t_t^s):

$$v^s = \frac{\lambda^s}{t_w^s + t_t^s} \tag{8}$$

As mentioned above, multiple types of precipitate and cluster (voids and loops) may appear in high Cr steel under irradiation. However, they are not expected to play a dominant role in the specific temperature and irradiation regimes (i.e. low dose and dose rate) considered in this work (Getto et al., 2017; Klueh, 2005). Therefore, their effects are ignored in what follows. As such, only dislocation type obstacle within the cell is accounted in the expression of λ^s. The hardening contributed by precipitates and clusters will be effectively included in the critical resolved shear stress (see below). The mean dislocation interspacing associated with dislocation-dislocation interactions can be given as Franciosi and Zaoui (1982):

$$\frac{1}{\lambda^s} = \sqrt{\sum_{s'} \bar{\alpha}^{ss'} \rho_{cell}^{s'}} \tag{9}$$

where $\bar{\alpha}^{ss'}$ refers to the latent hardening matrix. The dislocation waiting time can be described using the Kocks-type activation enthalpy law (Austin and McDowell, 2011; Kocks et al., 1975; Lloyd et al., 2014):

$$t_w^s = \begin{cases} \frac{1}{v^s} \exp\left(\frac{\Delta G_0}{kT}\left(1 - \left(\frac{|\tau_{\text{eff}}^s|}{\tau_c^s}\right)^p\right)^q\right) & \text{if } |\tau^s| < \tau_c^s \\ 0 & \text{if } |\tau^s| \geq \tau_c^s \end{cases} \tag{10}$$

here ΔG_0 is the thermal activation energy without any external stress. k is Boltzmann constant. T is the absolute temperature. $p(0 < p \leq 1)$ and $q(0 < q \leq 1)$ are the exponent parameters related to the shape of the obstacles resistance profile (Kocks et al., 1975). $v^s = \chi_e C_s/\lambda^s$ is the attack frequency, which is associated with the mean spacing between obstacles λ^s and the shear wave velocity C_s (Granato et al., 1964; Wang et al., 2017). χ_e is an entropy factor (of the order of 1). τ_c^s refers to the Critical Resolved Shear Stress (CRSS). Apart from the intrinsic frictional resistance τ_0^s, the net effect of all strengthening mechanisms can be expressed via use of a non-linear superposition law (Dong et al., 2010; Lagerpusch et al., 2000; Sobie et al., 2015). The sources accounted for in this work include precipitates, clusters, solute pinning, and the dislocations in the cell wall (through long-range stress field). However, the continuous evolution of the size and density of the precipitates and clusters under irradiation has not been quantified yet. Moreover, the solute pinning effect is also a complex matter due to the presence of multiple alloying elements, and the expressions proposed in the literature (Friedel, 1956; Labusch, 1970; Leyson and Curtin, 2016; Zaiser, 2002) do not apply to high-temperature regime. In this case, the hardening contribution from other sources, besides the dislocations in the cell wall, are treated as a temperature-dependent fitting parameter τ_h. Hence, we have:

$$\tau_c^s = \tau_0^s + (\tau_{cw}^n + \tau_h^n)^{1/n} \tag{11}$$

With $\tau_{cw} = \mu b^s \sqrt{\sum_s \bar{\alpha}^{ss'} \rho_{cw}^{s'}}$ denotes the cell wall-induced hardening, τ_h denotes the strengthening due to solute pinning and precipitates. τ_{eff}^s in Eq. 10 represents the effective driving stress acting on dislocations inside the cells. It is expressed as:

$$\tau_{\text{eff}}^s = \tau^s - \Delta\tau_m^s - \Delta\tau_l^s \tag{12}$$

here τ^s denotes the local resolved shear stress. $\Delta\tau_m^s$ and $\Delta\tau_l^s$ are associated with the local reduction in driving force acting on dislocations due to the presence of solutes and due to line tension respectively. Studies at atomistic scale observe that when an edge dislocation is pinned at obstacles, solute atoms can easily diffuse around the dislocation core (Leyson and Curtin, 2016; Soare and Curtin, 2008a, b). Consequently, this process will essentially increase the binding energy between the dislocation and its current position. This can be regarded as

an aging process that will effectively raise the stress required for the dislocation to unpin and can effectively control the strain rate sensitivity of the medium. The core-diffusion is associated with the time for solute to diffuse around the dislocation core, t_d, which effectively modulates the binding energy of the solute to the dislocation. The latter is given as:

$$\Delta E^{\text{core}}(t) = \Delta E_{\infty}^{\text{core}} \left(1 - exp\left(-\left(\frac{t}{t_d}\right)^{\varphi}\right)\right) \tag{13}$$

where $\Delta E_{\infty}^{\text{core}}$ is the saturation value for the binding energy. $\Delta\tau_m^s$ then can be written as:

$$\Delta\tau_m^s\left(t_{a,local}^s\right) = \frac{\alpha\Delta E^{\text{core}}\left(t_{a,local}^s\right)}{\bar{w}b^s} \tag{14}$$

$t_{a,local}^s$ is the local aging time (pinning period). α is associated with the energy variation along the core. $\bar{w}$ denotes the core width.

$\Delta\tau_l^s$ in Eq. 12 is the stress resulting from the dislocation curvature (i.e. line tension). As per Picu (Picu, 2004) who showed that solutes may also increase the effective dislocation-dislocation junction strength, $\Delta\tau_l^s$ is expected to depend on the aging history. Since a mobile dislocation may form junctions with any dislocation within the cell, the average junction strength of one grain is required. Therefore, the effective latent hardening matrix for each sub-material point is written as:

$$\bar{\alpha}_{local}^{ss\prime} = \alpha^{ss\prime}\left(1 + \frac{\chi\Delta E^{\text{core}}\left(t_{a,local}^{s\prime}\right)}{A}\right)^2 \tag{15}$$

where χ is a scaling parameter. Note that that the solute strengthening model used here was originally derived in (Leyson and Curtin, 2016; Soare and Curtin, 2008a, b) and applied to Aluminum. Although the present work focuses on BCC HT-9 steel, we believe the model is transferable, as the fundamental mechanisms (i.e. cross core diffusion) are driven by the stress fields around dislocations. With this, the effective latent hardening matrix can be determined through statistical averaging as follows (Wen et al., 2018):

$$\alpha^{ss\prime} = \int_{-\infty}^{\infty} \bar{\alpha}_{local}^{ss\prime}\ P(\tau^{s\prime} - \bar{\tau}^{s\prime}) d\tau^{s\prime} \tag{16}$$

and the line tension $\Delta\tau_l^s$ can be expressed as:

$$\Delta\tau_l^s = \mu b^s \sqrt{\sum_s \bar{\alpha}^{ss\prime} \rho_{cell}^{s\prime}} \tag{17}$$

2.2 Dislocation climb

Dislocation climb refers to the migration of edge dislocation segments perpendicular to their slip plane. It is a non-conservative process mediated by point defect absorption/emission. Under radiation environment, climb is promoted by the high density of vacancies and interstitials being created. Similar to Eq. 7, the local climb rate can also be expressed as an Orowan type equation. Notice that only edge dislocations contribute to the climb rate as:

$$\dot{\beta}^s = \rho_{cell,edge}^s b^s v_{climb}^s \tag{18}$$

here $\rho_{cell,edge}^s$ denotes the edge dislocation density. In BCC material, the nucleation of the double kink structure is frequent. Glide of edge (or screw) dislocations segments will result in the elongation of the screw (or edge) dislocation kinks. As a result of the faster motion of edge dislocations in BCC, their density is usually low. Following our previous study on Fe-Cr alloy (Wen et al., 2017), $\rho_{cell,edge}^s = 0.1\ \rho_{cell}^s$ is assumed in the simulations. v_{climb}^s in Eq. 18 represents the climb velocity, which depends on the net flux of point defects I_s. The climb velocity v_{climb}^s depends on the imbalance between vacancies and interstitials being trapped by the dislocation, which can be written using a classic expression of rate theory, as:

$$\bar{v}_c^s = \frac{\Omega}{b} I^s = \frac{\Omega}{b}\left(z_i^s D_i c_i^{sat} - z_v^s D_v (c_v^{sat} - c_v^0)\right) \tag{19}$$

where D_i and D_v denote the diffusivity for interstitial and vacancy. z_i^s and z_v^s are rate-theory parameters representing the dislocation capture efficiencies for interstitial and vacancy. $c_v^0 = c_v^{th}\, exp(\bar{\tau}_{climb}^s \Omega / kT)$ is the vacancy concentration around a dislocation at thermal equilibrium. $\Omega \approx b^3$ represents the atomic volume and c_v^{th} is the thermal equilibrium vacancy concentration. c_i^{sat} and c_v^{sat} are the saturation concentrations for interstitial and vacancy, respectively, under combined thermal and irradiation conditions. In fact, the

evolution of point defect concentration is a dynamic process that may affect the climb process, especially at the beginning of irradiation. However, because the saturation values are achieved nearly instantaneously in the temperature range considered, only c_i^{sat} and c_v^{sat} need to be considered in creep. In addition, for thermal creep the interstitial concentration is negligible and $c_v^{sat} = c_v^{th}$. In this case, the Eq. 19 reduces to:

$$\bar{v}_c^s = \frac{\Omega}{b}\left(z_v^s D_v c_v^{th}\left[\exp\left(\frac{\Omega\bar{\tau}_{climb}^s}{kT}\right) - 1\right]\right) \tag{20}$$

During irradiation, the saturation values of interstitial and vacancy depend on the sink strength. In this model, the stress and the dislocation density are not necessarily the same for each slip system. Therefore, the sink strength should be calculated at the slip system level. Assuming that point defects are homogeneously distributed and that dislocations are the predominant sink, the concentration rates for interstitial and vacancy in one grain are expressed as:

$$\dot{c}_i = K_0 - D_i c_i \sum_s (z_i^s \rho_{cell}^s) \tag{21}$$

and

$$\dot{c}_v = K_0 - D_v c_v \sum_s (z_v^s \rho_{cell}^s) + \sum_s \left(z_v^s \rho_{cell}^s \exp\left(\frac{\Omega\tau_{climb}^s}{kT}\right)\right) D_v c_v^{th} \tag{22}$$

Where, K_0 is the defect-pair creation rate per unit volume. K_0 is calculated here by multiplying the (most commonly reported) irradiation dpa-rate with the defect creation efficiency. The latter generally varies from 10% to 40%, depending on the material and recoil energy spectrum, and in this work we assume a value of 30% based on atomistic simulations of recoil cascades in Fe. (Bacon et al., 2003; Setyawan et al., 2015). Notice that only the dislocations in the cell are considered as sinks to point defects. The point defect recombination term is neglected here since its rate is negligible for all the saturation densities obtained in our calculations. At equilibrium conditions Eqs. (21) and (22) gives:

$$c_i^{sat} = \frac{K_0}{\sum_s (z_i^s \rho_{cell}^s) D_i} \tag{23}$$

and

$$c_v^{sat} = \frac{K_0 + \sum_s \left(z_v^s \rho^s \exp\left(\frac{\Omega \tau_{climb}^s}{kT} \right) \right) D_v c_v^{th}}{\sum_s (z_v^s \rho^s) D_v} \tag{24}$$

In the absence of thermal contributions, combining Eqs (20) through (24) gives

$$\bar{v}_c^s = \frac{K_0 \Omega}{b} \left[\frac{z_i^s}{\sum_m z_i^s \rho^m} - \frac{z_v^s}{\sum_m z_v^s \rho^m} \right] \tag{25}$$

which applies in the limit where irradiation defect densities are far larger than the thermal concentration.

The interstitial capture efficiency z_i^s is related to the stress as:

$$z_i^s = z_{i,0}^s + Z_{si} \bar{\tau}_{\text{climb}}^s \tag{26}$$

with $z_{i,0}^s$ the stress-free capture efficiency and Z_{si} is a scaling parameter for stress induced capture efficiency. On the other hand, because z_v^s has a much weaker dependence on stress (Heald and Speight, 1974), we have $z_v^s = z_{v,0}^s$. For cubic systems where defect diffusion is isotropic, the stress-free capture efficiencies are identical for all systems such that $z_{i,0}^s = z_i^0$. In this case, Eq (25) can be written

$$\bar{v}_c^s = \frac{K_0 \Omega}{b \rho} \left[\frac{1 + z_{si} \bar{\tau}_{climb}^s / z_i^0}{1 + \sum_m (Z_{si} \bar{\tau}_{climb}^m / z_i^0)(\rho^m / \rho)} - 1 \right], \tag{27}$$

which represents the SIPA contribution to climb, and vanishes in the case $Z_{si} = 0$. It is also evident from this expression that climb in the absence of alternative (non-dislocation) sinks and recombination scales linearly with the damage rate and is independent of the ratio between $z_i^0$and z_v^0.

2.3 Dislocation density evolution

The dislocation evolution law is essential to capture transient in the creep rate. The dislocation density affects the shear and climb rate on each slip system. Besides, the total dislocation density is required for the determination of the variance of the Gaussian stress distribution. In the present work, the dislocation density law previously developed for Fe-

Cr-Mo alloy is employed (Wen et al., 2017). High Cr steels usually form a subgrain structure during heat treatment (Abe, 2008). Therefore, the dislocation content can be divided into two populations: dislocations in the cell (subgrain) and in the cell walls (subgrain boundary). Notice that only the dislocations in the cell can move and contribute to the plastic deformation. The evolution of the dislocation density in the cell is expressed as:

$$\dot{\rho}^{s}_{\text{cell}} = \dot{\rho}^{s,+}_{\text{cell,g}} - \dot{\rho}^{s,-}_{\text{cell,a}} - \dot{\rho}^{s,-}_{\text{cell,trap}} \tag{28}$$

Where $\dot{\rho}^{s,+}_{\text{cell,g}}$, $\dot{\rho}^{s,-}_{\text{cell,a}}$, and $\dot{\rho}^{s,-}_{\text{cell,trap}}$ denotes the dislocation generation, dynamic recovery and trapping at the subgrain boundaries. The dislocation generation rate is associated with the area swept by the moving dislocations. The term $\dot{\rho}^{s,+}_{\text{cell,g}}$ can be expressed as (Kitayama et al., 2013; Wen et al., 2016):

$$\dot{\rho}^{s,+}_{\text{cell,g}} = \frac{k_1}{b\lambda^s}|\dot{\bar{\gamma}}^s| \tag{29}$$

Where $\frac{\lambda^s}{k_1}$ is the effective mean free path. The dynamic recovery involves several mechanisms, such as cross-slip and climb, that allow the dislocation to move to another slip plane and annihilate with dislocations with opposite Burger vector. Estrin (Estrin, 1998) proposed a general expression of the dynamic recovery rate:

$$\dot{\rho}^{s,-}_{\text{cell,a}} = k_2\left(\frac{\dot{\varepsilon}_0}{\dot{\varepsilon}}\right)^{\frac{1}{n_0}}\rho^{s}_{\text{cell}}|\dot{\bar{\gamma}}^s| \tag{30}$$

where $\dot{\varepsilon}_0$ is a reference strain rate. Estrin suggested that the parameter n_0 should be associated with the dominant mechanism (Estrin, 1998). Its value should be between 3 and 5 if it is a climb dominated process, or higher otherwise. The dislocation trapping rate at the subgrain boundaries is related to the subgrain size λ_{sg}:

$$\dot{\rho}^{s,-}_{\text{cell,trap}} = \frac{k_3}{\lambda_{\text{sg}}}|\dot{\bar{\gamma}}^s| \tag{31}$$

The trapped dislocations will essentially become part of the wall structure. Meanwhile, the dislocations in the cell wall will also annihilate. Thus, the rate of ρ^{s}_{cw} can be written as:

$$\dot{\rho}^{s}_{\text{cw}} = \dot{\rho}^{s,-}_{\text{cell,trap}} - \dot{\rho}^{s,-}_{\text{cw,a}} \tag{32}$$

Dislocation annihilation in the subgrain boundaries is complex and its mechanism for the Fe-Cr alloy is not fully understood. For the sake of simplicity, the annihilation rate is given here as follows:

$$\dot{\rho}_{\mathrm{cw,a}}^{s,-} = k_4 \rho_{cw}^{s} |\bar{\dot{\gamma}}^{s}| \tag{33}$$

The parameters k_1, k_2, k_3 and k_4 are material constants.

2.4 Coble creep

Besides dislocation motion, Coble creep may also contribute to plastic deformation in polycrystals via migration of point defects along grain boundaries. This mechanism usually takes place at high-temperature and low-stress and dictates a creep regime with stress exponent ≈ 1. Coble creep plays an essential role in the present work. In the experimental data of Toloczko et al. (Toloczko et al., 2001), the saturation creep rates under different conditions are linearly dependent on the imposed stress, indicating that steady-state creep is dominated by the Coble creep mechanism. According to (Coble, 1963), the creep law depends on the grain boundary width and grain boundary diffusion coefficient of vacancies or interstitials. In the present model, grain boundaries are not represented explicitly and grain boundary related material properties are known for the steel alloy system considered. Thus, Coble creep model written in simple form as,

$$\dot{\varepsilon}_{ij}^{coble} = \frac{A^{\mathrm{coble}} s_{ij}}{T} exp\left(-\frac{Q_{\mathrm{gb}}}{kT}\right) \tag{34}$$

where A^{coble} and Q_{gb} are effective parameters accounting for all point defects, and can be obtained through the fitting to the experimental data. s_{ij} denotes the ij component of the deviatoric stress tensor.

3 Creep simulations

To validate the proposed mechanistic model, thermal and irradiation creep simulations of ferritic/martensitic HT9 steel for a set of temperature and stresses are considered. The model predictions are compared against the experimental results reported in Toloczko et al. (Toloczko et al., 2001). The simulations are carried out within the VPSC framework by

assuming a rolled BCC initial texture as shown in Fig. 1. {110}⟨111⟩ and {112}⟨111⟩ systems are considered for both dislocation glide and climb. In Toloczko et al., pressurized tubes were used for both thermal and irradiation creep in the temperature range from 490°C to 600°C. In the present work, we have considered four sets of creep simulations: thermal creep at 490°C, 550°C and 600°C, and irradiation creep at 490°C. In the latter case thermal creep is also present. The required model parameters are fitted using only the thermal creep experimental data, and used for irradiation creep while adjusting only the parameter Z_{si}. The predicted and/or fitted HT9 model parameters are listed in Table 1.

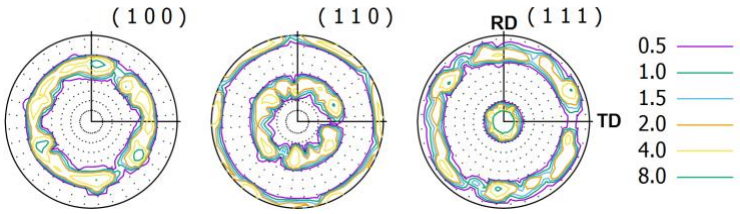

Figure 1: Initial texture of rolled BCC material. Directions RD and TD are equivalent to the axial and hoop directions in the HT-9 tube.

The initial dislocation density for HT9 material is currently unknown. Therefore, following our previous work on Fe-Cr alloy (Wen et al., 2017), we chose the initial values of ρ_{cell}^{s} and ρ_{cw}^{s} for each system to be $4{\cdot}10^{12}$ m^{-2} and $1{\cdot}10^{13}$ m^{-2}, respectively. The parameters ΔG_0, χ_e, p and q are determined by the back-fitting to experimental data within reasonable ranges ($\chi_e \approx 1$ (Wang et al., 2017); $0 < p \leq 1$ and $1 \leq p < 2$ (Kocks et al., 1975)). The hardening parameter τ_h is not accessible in existing studies. The work of (Gilbert et al., 2013) showed that the lattice friction τ_0^s in Fe decreases gradually with increasing temperature and vanishes at 427$_o$C. Thus, for the temperatures involved in this work, τ_0^s is set to be 0. The subgrain size λ_{sg} depends on ρ_{cw} following $1/\lambda_{sg} = \sqrt{\sum \beta^{ss'} \rho_{CW}^{s'}}$, here the $\beta^{ss'}$ is interaction coefficients. However, it is treated as constant in this work because: (a) ρ_{cw} does not vary evidently during creep, as shown later in section 4.1 and, (b) adopting explicit dependence would require one to introduce and fit the parameters $\beta^{ss\prime}$, for which there is no available experimental data.

The dislocation sink efficiencies $z^s_{i,0}$ and $z^s_{v,0}$ are chosen to be 1 and 1.2, which is within the reasonable range according to the literature. The SIPA parameter Z_{si} scales inversely with stiffness, and is poorly known due to uncertainty in the relevant point defect properties (chiefly the dia-elastic polarizability) and its dependence on multiple mechanisms (Matthews and Finnis, 1988). . Here, we tested the sensitivity of creep rate to its value (see Fig. 5), and settled on $Z_{si}= 0.3/\mu$ as the value that better captures the irradiation creep behavior measured in this system. The diffusivities of vacancies and interstitials are determined using molecular dynamics simulation data reported by (Mendelev and Mishin, 2009) for BCC Fe. The diffusivities of vacancy and interstitial are usually given by:

$$D_v = D_v^0 \exp\left(-E_m^v/kT\right)$$
$$D_i = D_i^0 \exp\left(-E_m^i/kT\right) \quad (35)$$

The migration energies E_m^v and E_m^i are 0.6 eV and 0.15 eV, respectively. The diffusion constants D_v^0 and D_i^0 are determined to be $7.87\times10^{-7}\,\mathrm{m^2/s}$ and $5.34\times10^{-8}\,\mathrm{m^2/s}$. The equilibrium vacancy concentration can be expressed as (Was, 2016):

$$C_v^0 = \exp\left(-\frac{G_f}{kT}\right) \quad (36)$$

with G_f is the Gibbs energy of vacancy formation and is taken as 2.0eV. Note that G_f is temperature dependent, but the depedency is relatively weak at high temperature, and so we assume a constant value.

Table 1. Parameters used for HT-9 in this work

Parameters	**HT9 parameters**
b (magnitude of Burgers vector)	$2.48\cdot10^{-10}$ m
μ (shear modulus)	103572 MPa-T·48 MPa/K
τ_0 (friction stress)	0 MPa
τ_h (hardening contribution from solute pinning and precipitation)	220 MPa (490°C) 208 MPa (550°C) 201 MPa (600°C)
η (scaling parameter)	$1.73\cdot10^{-6}$ MPa/m

ΔG_0 (zero-stress activation energy for dislocations)	3 eV
p (exponent parameter)	0.9
q (exponent parameter)	1.1
χ_e (entropy factor)	0.5
$\rho_{cell,0}^s$ (initial dislocation density in the cell)	$4 \cdot 10^{12}$ m^{-2}
$\rho_{cw,0}^s$ (initial dislocation density in the cell wall)	$1 \cdot 10^{13}$ m^{-2}
k_1 (material constant)	0.033
k_2 (material constant)	31.5
k_3 (material constant)	$1.5 \cdot 10^8$
k_4 (material constant)	600
λ_{sg} (sub-grain size)	$0.5 \cdot 10^{-6}$m
n_0 (annihilation strain rate sensitivity)	3.5
$\dot{\varepsilon}_0$ (reference strain rate)	1 s^{-1}
n (superposition power)	2.22
φ (power parameter)	1
$\overline{w}$ (width of dislocation core)	1.86 nm
χ (pre-factor linking binding energy and junction strength)	5
α (scaling coefficient for $\Delta\tau_m^s$)	0.38
$\alpha_0^{ss'}$ (saturation dislocation-dislocation interaction)	0.7 ($s = s'$); 0.05 ($s \neq s'$)
D_v^0 (vacancy diffusion constant)	$7.87 \cdot 10^{-7}$ m^2/s
E_m^v (vacancy migration energy)	0.6 eV
D_i^0 (interstitial diffusion constant)	$5.34 \cdot 10^{-8}$ m^2/s
E_i^v (vacancy migration energy)	0.15 eV
G_f (Gibbs energy of vacancy formation)	2.0 eV
A^{coble} (Coble creep parameter)	$8.0 \cdot 10^{-8}$
Q_{gb} (Coble creep parameter)	0.37eV

4 Results and discussion

In Toloczko et al. (Toloczko et al., 2001), pressurized thin walled tubes (diameter/thickness = 22.85 > 20) were used for both thermal and irradiation creep. The pressure-induced stress tensor can be written as,

$$[\sigma] = \begin{bmatrix} \sigma_A & 0 & 0 \\ 0 & \sigma_H & 0 \\ 0 & 0 & 0 \end{bmatrix} \tag{37}$$

Where σ_H and $\sigma_A = \sigma_H/2$ denote the hoop and axial stress. In their work, the imposed stress and the measured creep strains are represented in terms of von-Mises stress, $\bar{\sigma} = \sqrt{\frac{3}{2}\boldsymbol{\sigma}_{ij}:\boldsymbol{\sigma}_{ij}}$ and von-Mises strain, $\bar{\varepsilon} = \sqrt{\frac{2}{3}\boldsymbol{\varepsilon}_{ij}:\boldsymbol{\varepsilon}_{ij}}$, respectively. Accordingly, hoop stress and strain component can we written as $\sigma_H = \frac{2}{\sqrt{3}}\bar{\sigma}$ and $\varepsilon_H = \frac{\sqrt{3}}{2}\bar{\varepsilon}$.

4.1 Thermal creep

Thermal creep simulations of HT9 steel are performed using the affine-VPSC formulation (Lebensohn et al., 2007) for three different temperatures, namely, 490°C, 500°C and 600°C. For each temperature case, three different von-Mises stresses are considered: for 480°C: 87, 121 and 173 MPa; for 550°C: 52, 87 and 121 MPa; and for 600°C: 9, 39 and 66 MPa. The creep behavior predicted by the model for all three temperature cases is reported in Figure 2, and clearly shows that the proposed model captures the thermal creep behavior correctly for all stress and temperature cases. This validates the proposed mechanistic model for thermal creep behavior. Note that the primary–to-secondary transition spans approximately 60 hours for all the cases, during which interval a considerable amount of creep strain takes place. The latter points at potential limitations and underestimates when utilizing constitutive creep laws describing only the steady state creep.

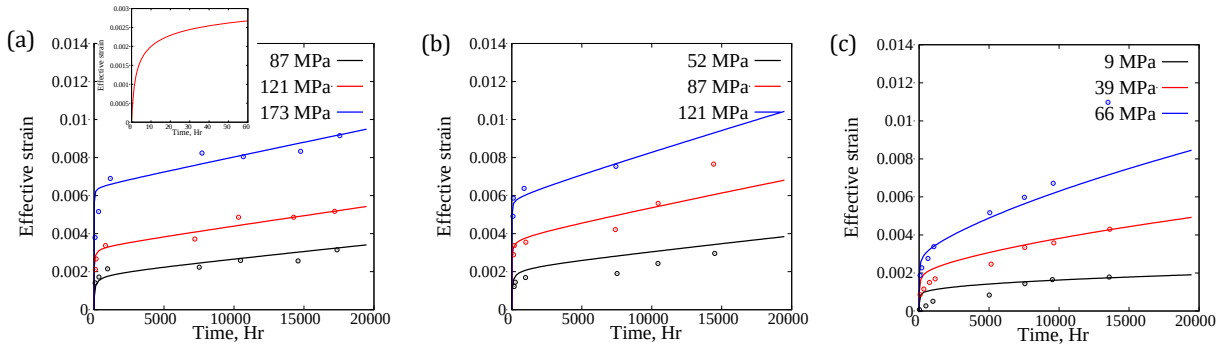

Figure 2. Predicted thermal creep behavior of HT9 steel as a function of von-Mises stresses at (a) 490°C, (b) 550°C and (c) 600°C. The empty circles are the experimental measurements taken from (Toloczko et al., 2001). The proposed model captures creep responses for a wide range of stress and temperature. Figure insert in (a) shows the primary-to-secondary transition in creep response for 480 °C and 121 MPa case.

Further, to understand the deformation mechanisms that contribute to the predicted creep rates, the relative contribution of glide, climb and Coble creep modes are plotted in Figure 3 as the microstructure evolves. At the early state of creep, mostly glide mechanism alone contribute to the creep rate for all stress and temperature cases. After a few hours, the contribution of glide decreases rapidly, while climb and Coble modes start to activate. The reduction in glide mode can be explained by the evolution dislocation densities in the cell. For that purpose, the evolution of dislocation densities within the cell and in the cell-wall is shown in Figure 4 for all the cases. Within a few hours, the dislocation density in the cell decreases rapidly and reaches the saturation limit. The cell dislocation density profile resembles the glide mode contribution profile (see Figure 3). The reduction of dislocation density within the cell is significant for the 600°C case, compared to 490°C and 550°C, due to temperature dependent annihilation of dislocations.

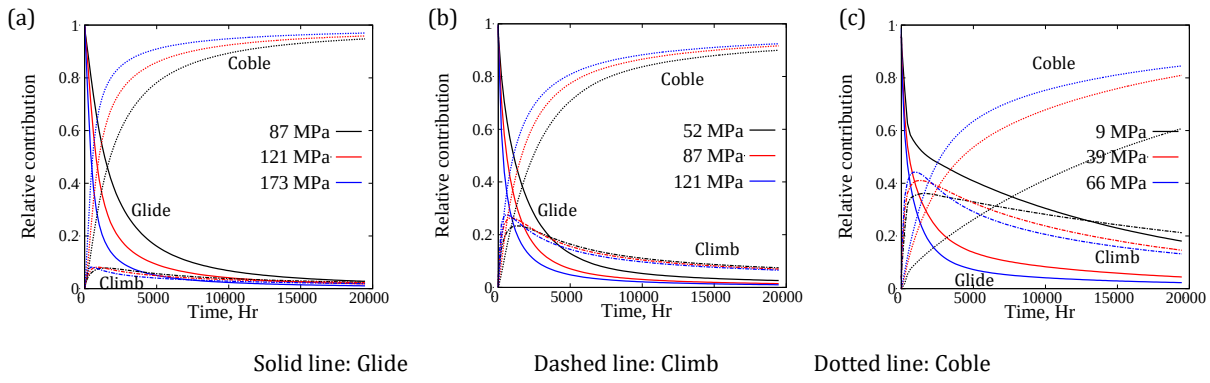

Figure 3. Relative contribution of individual mechanisms (glide, climb and Coble) on creep rate as a function of von-Mises stress at (a) 490°C, (b) 550°C and (c) 600°C. Glide and Coble creep dominate in the primary and steady state regimes, respectively. Increasing temperature increases the climb contribution to plasticity.

For all three temperatures, the contribution of Coble creep increases rapidly almost at the same rate at which the glide contribution decreases, and becomes the dominant mechanism at the steady-state regime. The climb contribution increases with increasing temperature. Particularly, its contribution at 490°C is almost negligible and becomes significant at higher temperatures. In summary, at lower temperature (say 490°C) dislocation glide and Coble creep modes dominate the primary and secondary creep regimes, respectively. On the other hand, for high temperature (550°C and 600°C), dislocation glide, and both climb and Coble creep contributes to the primary and secondary creep regimes, respectively.

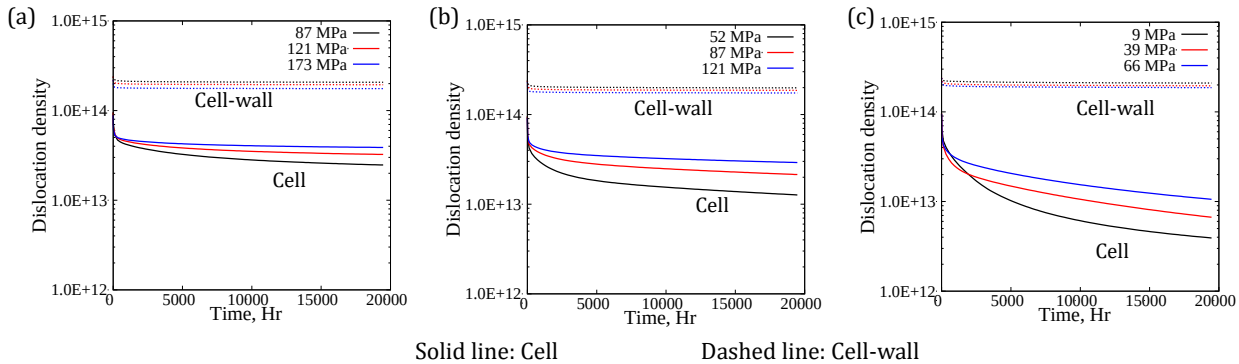

Figure 4. Evolution of dislocation densities in the cell and in the cell-wall as a function of von-Mises stress at (a) 490°C, (b) 550°C and (c) 600°C. The dislocation densities in the cell-wall do not change much in both primary and secondary creep regimes. At the primary creep regime, dislocation densities in the cell decrease rapidly and thus limit the glide contribution to creep rate.

4.2 Irradiation creep

In this work, we have performed irradiation creep simulation at 490°C for three different von-Mises stresses (52MPa, 87MPa and 121 MPa). In (Toloczko et al., 2001), irradiation creep tests are performed at a dose rate of ~0.8 x 10^{-6} dpa/sec. Accordingly, the defect-pair creation rate in Eq. 22 is 1.573 x 10^{22} m^{-3} s^{-1}. As mentioned previously, all the model parameters that are fitted against thermal creep behavior are directly used here., Note that the term Z_{si} is inversely proportional to material stiffness (Matthews and Finnis, 1988). Accordingly, we have performed creep simulations for $Z_{si} = 0.0$, $0.3/\mu$ and $0.6/\mu$. When assuming $Z_{si} = 0$, the irradiation induced creep in this model vanishes, as illustrated in Eq. 26. Among all the fitted parameters, one can argue that the precipitation hardening term τ_h may be altered due to the creation of irradiation-induced barriers. But the temperature that we consider for creep simulations is in the regime where the irradiation induced hardening is almost negligible (Klueh, 2005).

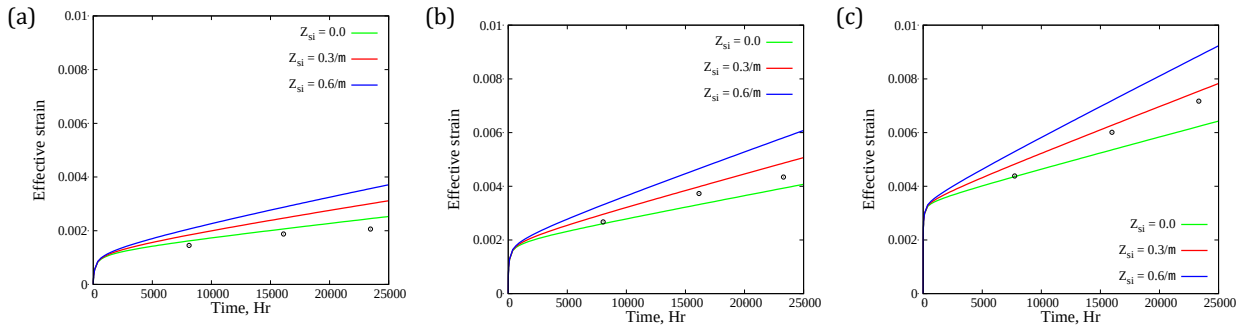

Figure 5. Predicted irradiation creep behavior of HT9 steel at 490°C and (a) 52 MPa, (b) 87 MPa and (c) 121 MPa. The empty circles are the experimental measurements taken from

(Toloczko et al., 2001). Three different scaling parameters are used for interstitial efficiency, see Eq. 26, namely: $Z_{si} = 0.0$, $Z_{si} = 0.3/\mu$ and $Z_{si} = 0.6/\mu$.

Figure 5 shows the predicted irradiation creep response for all three von-Mises stress cases at 490°C along with experimental data from (Toloczko et al., 2001). By comparing the predicted and measured responses, it is apparent that $Z_{si} = 0.3/\mu$ captures best the effect of temperature and stresses on irradiation creep and is a reasonable value for this material. However, it has to be kept in mind that this value is conditioned by the assumptions made, such as (1) irradiation induced change in precipitate hardening is negligible, and (2) efficiency of defect-pair creation rate is 30%. To understand the plastic mechanisms that contribute to the predicted creep response, the relative contribution of glide, climb and Coble creep modes are plotted in Figure 6 for all three stress cases. Similar to thermal creep calculations, both glide and Coble creep modes contribute majorly at the primary and secondary creep regimes, respectively. As was to be expected, climb contributes more for the case of irradiation compared to thermal creep for the same temperature and stress range (compare Figure 3(a) and Figure 6). The climb contribution in thermal creep at 490°C for all stresses is less than 10%. But during irradiation creep, climb contributes to a maximum of ~35%. In addition to that, the contribution of climb is also strongly dependent on the term Z_{si}, as seen in Figure 6.

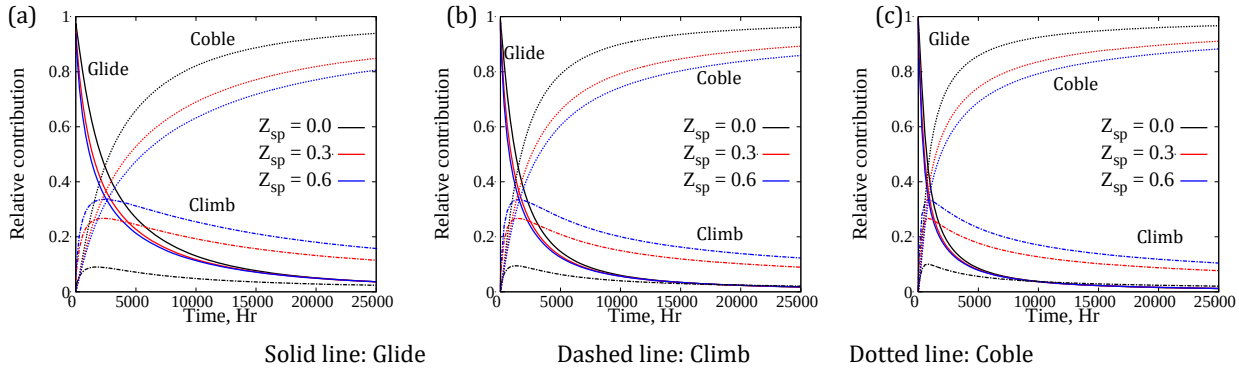

Figure 6. Relative contribution of individual mechanisms (glide, climb and Coble) on creep rate as a function of scaling parameter, Z_{sp}, at 490°C and (a) 52 MPa, (b) 87 MPa and (c) 121 MPa.

Compared to thermal creep at same temperature and stress level, the activation of climb is significant under irradiation creep.

5 Summary

In this work a mechanism-based model is proposed to predict the thermal and irradiation creep behavior of HT-9. The focus is placed on the development of a rate-theory-based dislocation climb law while considering the contribution of irradiation-induced point defects. The novel climb approach is coupled with a constitutive model describing the effects of solute strengthening and Coble creep mechanisms. The proposed model is benchmarked using the experimental results of (Toloczko et al., 2001) for both thermal and irradiation creep tests. The simulation results indicate that the proposed model can quantitatively assess the relative roles of the physical mechanisms and demonstrate their effects on the macroscopic behavior, as revealed in experimental data., Specifically, the model captures well the experimental creep strains, the separate contribution of climb and Coble creep modes and, more interestingly, the irradiation-induced climb contribution to the overall creep response.

From this work it becomes apparent the complexity associated with simultaneously acting mechanisms and their coupling. Such complexity leads to a large number of parameters that need to be characterized. Some can be derived from first principle calculations, while others are calibrated through the back-fitting to the macroscopic experimental data within reasonable ranges. This process may introduce uncertainties in the description of each individual mechanism. The core-diffusion process and the non-conservative dislocation climb in HT9 steel require further study for this specific alloy. Atomistic simulations will be carried out in the future to enhance our understanding of these mechanisms and provide more accurate parameter calibration. Another major unknown of this work is the precipitation process of HT9, which is associated with the fabrication process, temperature and irradiation dosage. A systematic investigation will be necessary to

determine the size and density evolution of the precipitates under both thermal and irradiation environments.

Acknowledgements

This work was funded by the US Department of Energy's Nuclear Energy Advanced Modeling and Simulation (NEAMS).

References

Abe, F., 2008. Precipitate design for creep strengthening of 9% Cr tempered martensitic steel for ultra-supercritical power plants. Science and Technology of advanced materials 9, 013002.
Anderoglu, O., Van den Bosch, J., Hosemann, P., Stergar, E., Sencer, B., Bhattacharyya, D., Dickerson, R., Dickerson, P., Hartl, M., Maloy, S., 2012. Phase stability of an HT-9 duct irradiated in FFTF. J Nucl Mater 430, 194-204.
Austin, R.A., McDowell, D.L., 2011. A dislocation-based constitutive model for viscoplastic deformation of fcc metals at very high strain rates. Int J Plasticity 27, 1-24.
Bacon, D.J., Osetsky, Y.N., Stoller, R., Voskoboinikov, R.E., 2003. MD description of damage production in displacement cascades in copper and α-iron. J Nucl Mater 323, 152-162.
Briggs, S.A., Edmondson, P.D., Littrell, K.C., Yamamoto, Y., Howard, R.H., Daily, C.R., Terrani, K.A., Sridharan, K., Field, K.G., 2017. A combined APT and SANS investigation of α' phase precipitation in neutron-irradiated model FeCrAl alloys. Acta Mater 129, 217-228.
Bullough, R., Willis, J.R., 1975. The stress-induced point defect-dislocation interaction and its relevance to irradiation creep. Philos Mag 31, 855-861.
Chen, W.-Y., Miao, Y., Wu, Y., Tomchik, C.A., Mo, K., Gan, J., Okuniewski, M.A., Maloy, S.A., Stubbins, J.F., 2015. Atom probe study of irradiation-enhanced α' precipitation in neutron-irradiated Fe–Cr model alloys. J Nucl Mater 462, 242-249.
Coble, R., 1963. A model for boundary diffusion controlled creep in polycrystalline materials. J Appl Phys 34, 1679-1682.
Dong, Y., Nogaret, T., Curtin, W., 2010. Scaling of dislocation strengthening by multiple obstacle types. Metallurgical and Materials Transactions A 41, 1954-1960.
Dubuisson, P., Gilbon, D., Séran, J., 1993. Microstructural evolution of ferritic-martensitic steels irradiated in the fast breeder reactor Phénix. J Nucl Mater 205, 178-189.
Edmondson, P.D., Briggs, S.A., Yamamoto, Y., Howard, R.H., Sridharan, K., Terrani, K.A., Field, K.G., 2016. Irradiation-enhanced α' precipitation in model FeCrAl alloys. Scripta Mater 116, 112-116.
Ehrlich, K., 1981. Irradiation creep and interrelation with swelling in austenitic stainless steels. J Nucl Mater 100, 149-166.
Estrin, Y., 1998. Dislocation theory based constitutive modelling: foundations and applications. Journal of Materials Processing Technology 80, 33-39.
Field, K.G., Briggs, S.A., Littrell, K., Parish, C.M., Yamamoto, Y., 2016. Database on Performance of Neutron Irradiated FeCrAl Alloys. Oak Ridge National Laboratory (ORNL), Oak Ridge, TN (United States). Center ….

Field, K.G., Hu, X., Littrell, K.C., Yamamoto, Y., Snead, L.L., 2015. Radiation tolerance of neutron-irradiated model Fe–Cr–Al alloys. J Nucl Mater 465, 746-755.
Foster, J., Wolfer, W., Biancheria, A., Boltax, A., 1972. Analysis of irradiation-induced creep of stainless steel in fast spectrum reactors. Westinghouse Electric Corp., Madison, Pa.(USA). Advanced Reactors Div.
Friedel, J., 1956. Les dislocations, Gauthier-Villars, Paris. 1956.
Garner, F., 1994. Irradiation performance of cladding and structural steels in liquid metal reactors, Vol. 10A of Materials Science and Technology: A Comprehensive Treatment. VCH Publishers.
Getto, E., Vancoevering, G., Was, G., 2017. The co-evolution of microstructure features in self-ion irradiated HT9 at very high damage levels. J Nucl Mater 484, 193-208.
Gilbert, M., Schuck, P., Sadigh, B., Marian, J., 2013. Free energy generalization of the Peierls potential in iron. Phys Rev Lett 111, 095502.
Granato, A., Lücke, K., Schlipf, J., Teutonico, L., 1964. Entropy factors for thermally activated unpinning of dislocations. J Appl Phys 35, 2732-2745.
Groma, I., Bakó, B., 1998. Probability distribution of internal stresses in parallel straight dislocation systems. Phys Rev B 58, 2969.
Groma, I., Székely, F., 2000. Analysis of the asymptotic properties of X-ray line broadening caused by dislocations. Journal of applied crystallography 33, 1329-1334.
Heald, P., Speight, M., 1974. Steady-state irradiation creep. Philos Mag 29, 1075-1080.
Kai, J., Klueh, R., 1996. Microstructural analysis of neutron-irradiated martensitic steels. J Nucl Mater 230, 116-123.
Kitayama, K., Tomé, C., Rauch, E., Gracio, J., Barlat, F., 2013. A crystallographic dislocation model for describing hardening of polycrystals during strain path changes. Application to low carbon steels. Int J Plasticity 46, 54-69.
Klueh, R., 2005. Elevated temperature ferritic and martensitic steels and their application to future nuclear reactors. International Materials Reviews 50, 287-310.
Kocks, U.F., Argon, A.S., Ashby, M.F., 1975. Thermodynamics and kinetics of slip. Prog Mater Sci 19, 171-229.
Labusch, R., 1970. A statistical theory of solid solution hardening. physica status solidi (b) 41, 659-669.
Lagerpusch, U., Mohles, V., Baither, D., Anczykowski, B., Nembach, E., 2000. Double strengthening of copper by dissolved gold-atoms and by incoherent SiO2-particles: how do the two strengthening contributions superimpose? Acta Mater 48, 3647-3656.
Lebensohn, R., Tomé, C., Castaneda, P.P., 2007. Self-consistent modelling of the mechanical behaviour of viscoplastic polycrystals incorporating intragranular field fluctuations. Philos Mag 87, 4287-4322.
Lebensohn, R.A., Hartley, C.S., Tomé, C.N., Castelnau, O., 2010. Modeling the mechanical response of polycrystals deforming by climb and glide. Philos Mag 90, 567-583.
Lebensohn, R.A., Tome, C.N., 1993. A Self-Consistent Anisotropic Approach for the Simulation of Plastic-Deformation and Texture Development of Polycrystals - Application to Zirconium Alloys. Acta Metallurgica Et Materialia 41, 2611-2624.
Leyson, G., Curtin, W., 2016. Solute strengthening at high temperatures. Model Simul Mater Sc 24, 065005.
Lloyd, J., Clayton, J., Austin, R., McDowell, D., 2014. Plane wave simulation of elastic-viscoplastic single crystals. J Mech Phys Solids 69, 14-32.

Maloy, S.A., Saleh, T.A., Anderoglu, O., Romero, T.J., Odette, G.R., Yamamoto, T., Li, S., Cole, J.I., Fielding, R., 2016. Characterization and comparative analysis of the tensile properties of five tempered martensitic steels and an oxide dispersion strengthened ferritic alloy irradiated at≈ 295° C to≈ 6.5 dpa. J Nucl Mater 468, 232-239.
Matthews, J., Finnis, M., 1988. Irradiation creep models—An overview. J Nucl Mater 159, 257-285.
Mendelev, M.I., Mishin, Y., 2009. Molecular dynamics study of self-diffusion in bcc Fe. Phys Rev B 80, 144111.
Pastore, G., Novascone, S., Williamson, R., Hales, J., Spencer, B., Stafford, D., 2015. Modelling of fuel behaviour during loss-of-coolant accidents using the BISON code. Idaho National Lab.(INL), Idaho Falls, ID (United States).
Picu, R., 2004. A mechanism for the negative strain-rate sensitivity of dilute solid solutions. Acta Mater 52, 3447-3458.
Rogozhkin, S., Korchuganova, O., Aleev, A., 2016. Kinetics of α'-phase nucleation during thermal aging of Fe–22% Cr alloy. Inorganic Materials: Applied Research 7, 210-213.
Sencer, B.H., Kennedy, J., Cole, J., Maloy, S.A., Garner, F.A., 2009. Microstructural analysis of an HT9 fuel assembly duct irradiated in FFTF to 155 dpa at 443 C. J Nucl Mater 393, 235-241.
Setyawan, W., Selby, A.P., Juslin, N., Stoller, R.E., Wirth, B.D., Kurtz, R.J., 2015. Cascade morphology transition in bcc metals. Journal of Physics: Condensed Matter 27, 225402.
Soare, M., Curtin, W., 2008a. Single-mechanism rate theory for dynamic strain aging in fcc metals. Acta Mater 56, 4091-4101.
Soare, M., Curtin, W., 2008b. Solute strengthening of both mobile and forest dislocations: The origin of dynamic strain aging in fcc metals. Acta Mater 56, 4046-4061.
Sobie, C., Bertin, N., Capolungo, L., 2015. Analysis of obstacle hardening models using dislocation dynamics: application to irradiation-induced defects. Metallurgical and Materials Transactions A 46, 3761-3772.
Toloczko, M., Grambau, B., Garner, F., Abe, K., 2001. Comparison of Thermal Creep and Irradiation Creep of HT9 Pressurized Tubes at Test Temperatures from~ 490° C to 605° C, Effects of Radiation on Materials: 20th International Symposium. ASTM International.
Uehira, A., Mizuta, S., Ukai, S., Puigh, R., 2000. Irradiation creep of 11Cr–0.5 Mo–2W, V, Nb ferritic–martensitic, modified 316, and 15Cr–20Ni austenitic SS irradiated in FFTF to 103–206 dpa. J Nucl Mater 283, 396-399.
Wang, H., Capolungo, L., Clausen, B., Tomé, C., 2017. A crystal plasticity model based on transition state theory. Int J Plasticity 93, 251-268.
Wang, H., Clausen, B., Capolungo, L., Beyerlein, I.J., Wang, J., Tome, C.N., 2016. Stress and strain relaxation in magnesium AZ31 rolled plate: In-situ neutron measurement and elastic viscoplastic polycrystal modeling. Int J Plasticity 79, 275-292.
Was, G.S., 2016. Fundamentals of radiation materials science: metals and alloys. Springer.
Wen, W., Borodachenkova, M., Tomé, C., Vincze, G., Rauch, E., Barlat, F., Grácio, J., 2016. Mechanical behavior of low carbon steel subjected to strain path changes: Experiments and modeling. Acta Mater 111, 305-314.
Wen, W., Capolungo, L., Patra, A., Tome, C.N., 2017. A Physics-Based Crystallographic Modeling Framework for Describing the Thermal Creep Behavior of Fe-Cr Alloys. Metall Mater Trans A 48a, 2603-2617.

Wen, W., Capolungo, L., Tomé, C.N., 2018. Mechanism-based modeling of solute strengthening: Application to thermal creep in Zr alloy. Int J Plasticity 106, 88-106.
Wilkens, M., 1970. The determination of density and distribution of dislocations in deformed single crystals from broadened X‐ray diffraction profiles. Physica status solidi (a) 2, 359-370.
Woo, C., 1984. Irradiation creep due to elastodiffusion. J Nucl Mater 120, 55-64.
Zaiser, M., 2002. Dislocation motion in a random solid solution. Philosophical Magazine A 82, 2869-2883.
Zheng, C., Auger, M.A., Moody, M.P., Kaoumi, D., 2017. Radiation induced segregation and precipitation behavior in self-ion irradiated Ferritic/Martensitic HT9 steel. J Nucl Mater 491, 162-176.